Available at www.sciencedirect.com

ScienceDirect

journal homepage: www.elsevier.com/locate/he

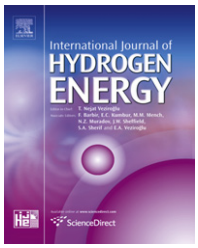

Influence of machining-induced martensite on hydrogen-assisted fracture of AISI type 304 austenitic stainless steel

M. Martin [a], S. Weber [a,b,*], C. Izawa [c], S. Wagner [c], A. Pundt [c], W. Theisen [a]

[a] Ruhr-Universität Bochum, Institut für Werkstoffe, Lehrstuhl Werkstofftechnik, D-44780 Bochum, Germany
[b] Helmholtz-Zentrum Berlin für Materialien und Energie GmbH, D-14109 Berlin, Germany
[c] Georg-August-Universität Göttingen, Institut für Materialphysik, D-37077 Göttingen, Germany

ARTICLE INFO

Article history:
Received 25 February 2011
Accepted 21 May 2011
Available online 7 July 2011

Keywords:
Austenitic stainless steel
Hydrogen-assisted fracture
Surface condition
Machining
Strain-induced martensite
SIMS

ABSTRACT

Hydrogen-assisted fracture of AISI type 304 steel has been evaluated with a special focus on the strain-induced martensite that is produced below the specimen surface during standard turning operation. Two different surface conditions were investigated: one containing martensite, resulting from the machining process, and a martensite-free state which is obtained after a proper heat treatment. Additionally, chemical composition and thickness of oxide layers, occurring in both studied cases, were analyzed by secondary ion mass spectrometry. These two different conditions were tested at room temperature in air (ambient pressure) and in hydrogen gas (40 MPa) atmosphere, respectively. Experimental results reveal a detrimental effect of machining-induced martensite on AISI type 304 steel performance in hydrogen, leading to major differences in relative reduction of area (RRA) between the as-machined and the heat-treated state for the same material. In this context, an operating mechanism based on hydrogen diffusion is discussed.

1. Introduction

Hydrogen gas storage and hydrogen use in mobile applications are related to hydrogen environment embrittlement (HEE), a phenomenon characterized by a deterioration of mechanical properties caused by the presence of external hydrogen gas. Austenitic stainless steels are frequently used for hydrogen applications due to their high ductility at low temperatures, low thermal conductivity and lower HEE compared to ferritic steels. AISI type 304 steel is the most commonly used austenitic stainless steel in general. It is often tested in the context of HEE: On the one hand for comparison with existing materials or new alloys and on the other hand due to its relatively low cost. The requirement of low costs has generated an interest in HEE of austenitic stainless steels with moderate nickel content in the range of 8–10 wt.%. In this group of steels, the resistance against HEE decreases with decreasing nickel content [1]. In order to provide a cost-effective solution, AISI type 304 steel parts are usually produced by standard cutting and turning processes which can be accompanied by the formation of strain-induced martensite at the machined surface. The intention of the present work is to elucidate the influence of present phases and microstructure at the surface on hydrogen-assisted fracture. To evaluate the influence of machining-induced martensite it is helpful to survey the possible interactions of hydrogen and austenitic stainless steels first.

* *Corresponding author*. Helmholtz-Zentrum Berlin für Materialien und Energie GmbH, D-14109 Berlin, Germany.
E-mail address: sebastian.weber@helmholtz-berlin.de (S. Weber).
0360-3199/$ – see front matter
doi:10.1016/j.ijhydene.2011.05.133

1.1. Austenite stability

For HEE of austenitic stainless steels a relation of embrittlement and austenite stability is found in literatures [2,3]. Austenite stability describes the resistance of austenitic stainless steel to transform its fcc structure to either α- or ϵ-martensite, the latter being found preferentially in Cr–Mn austenitic stainless steels due to cooling and/or deformation [4]. While ϵ-martensite is supposed to play a minor role for HEE [5,6], the formation of α-martensite with tetragonally distorted bcc structure supports the embrittlement effect significantly [7]. The latter effect arises from the diffusivity of hydrogen in the bcc lattice, being orders of magnitude higher compared to fcc iron [8]. It can thus be assumed, that HEE of conventional Cr–Ni austenitic stainless steels is proportional to their austenite stability. Han et al. investigated AISI type 304, 316 and 310S austenitic stainless steels in solution-annealed, sensitized and desensitized condition in the temperature range from 295 to 80 K. The sensitized heat treatment condition is related to a loss in wet corrosion resistance due to the precipitation of chromium rich carbides along grain boundaries. Results in hydrogen at a gas pressure of 100 kPa are compared to those obtained in helium at the same pressure [9]. First of all, no HEE was found for 310S in the different heat treatment states and all temperatures as a result of its high austenite stability. Severe HEE was found at about 220 K for 304 and 316, for the latter in the sensitized condition. The authors relate the influence of sensitization to a reduction of austenite stability due to the precipitation of carbides along grain boundaries, as only carbon in solid solution is able to stabilize the fcc structure. In case of a sufficient austenite stability due to the chemical composition, like for 310S, a reduction by carbide precipitation does not play a role for HEE. However, along carbon depleted zones the formation of strain-induced martensite is enhanced, leading to a brittle failure in the presence of hydrogen. Perng and Altstetter investigated hydrogen embrittlement of AISI 300 series at 108 kPa compared to high-manganese austenitic steels [10]. They found least HEE for an Fe–C–Al–Mn alloy and related this result to a high austenite stability. At first view, their results obtained for the Fe–C–Al–Mn alloy are in contrast to findings of Michler et al., who investigated HEE of stable high-Mn austenitic stainless steels arising from the system Fe–Cr–Mn–N [11]. The latter authors discovered severe HEE during tensile testing of these high-Mn austenitic stainless steels at 220 K. However, the only common feature of both materials, Fe–C–Al–Mn and Fe–Cr–Mn–N, is the high content of manganese and the fully stable austenitic structure, while the alloy system is completely different. According to Zhang et al., the brittle failure of high-Mn austenitic stainless steels can be attributed to their low stacking fault energy (SFE) as it induces slip planarity [12]. In general, the work of the latter authors supports the assumption of austenite stability to play a major role for HEE. They investigated eleven different austenitic stainless steels based on AISI 316 in the temperature range of 80 K–300 K and changed the nickel equivalent keeping the contents of other alloying elements constant. At the most critical temperature of 200 K a threshold value of nickel equivalent of about 10 wt.% was found. Above this value, as a result of the higher stability of the fcc phase to transform to α-martensite, no HEE was found during tensile testing in 100 kPa hydrogen gas with a strain rate of $4.2 \cdot 10^{-5}$ s^{-1}.

1.2. Microstructural mechanisms

It is worth mentioning, that a joint movement of dislocations and hydrogen clouds is assumed by several authors as a prerequisite for hydrogen embrittlement [13,14]. This could serve as an explanation for the strong influence of strain rate on HEE, that is not found in high strain rate experiments [13,15]. The interaction of hydrogen with dislocations also explains the minimum in relative reduction of area (RRA) as a function of testing temperature. For temperatures below a critical value, hydrogen diffusivity is too low to allow it to follow dislocations [16]. At higher temperatures no α-martensite is formed. This can be attributed to the M_d temperature and a higher SFE. Additionally, the contribution of entropy hinders hydrogen to accumulate in the stress field of dislocations at elevated temperature [16].

1.3. Surface condition

In ambient atmosphere austenitic stainless steels are passivated immediately by the formation of chromium oxide and iron oxide layers. For type 304 stainless steel, semiconducting behavior of these oxide layers was found [17]. Surface oxide layers usually serve as a barrier for hydrogen dissociation and dissolution in gaseous hydrogen environments [18]. The protective function of the oxide layer against hydrogen uptake is restricted to molecular hydrogen, that needs to dissociate to enter the crystal lattice. To allow gaseous hydrogen to enter the material three prerequisites are necessary: the adsorption of molecular hydrogen, its dissociation at the surface and finally the dissolution to interstitial sites [19,20]. Due to the existence of the passivation layer, at least the second step is kinetically hindered. The situation is changed once the passivation layer is damaged. During tensile testing in high purity hydrogen at low oxygen partial pressure, the passivation layer is destroyed and fresh metal surface formed providing local areas for hydrogen to be absorbed. On the contrary, when testing in hydrogen of lower purity and higher oxygen partial pressures, less hydrogen environment embrittlement is encountered [21]. This finding can be related to the re-passivation of the surface that acts as an effective barrier for hydrogen dissociation. Fracture of oxide by tensile testing also occurs in artificial oxide layers that can be obtained by wet corrosion, high temperature treatment or oxidation in plasma. The latter approach was used by Michler et al. who investigated the influence of different coatings on HEE of 304 austenitic steels [22]. For the artificially oxidized samples no improvement of HEE was found and related to the formation of small cracks and delamination of the oxide layer.

1.4. Outline

Based on these informations one might assume a minor role of the surface microstructure on the overall mechanical

properties measured in gaseous hydrogen, as the contribution of a comparatively thin surface layer to the volume of the sample is small. However, as already stated, it is known that α-martensite is detrimental for HEE but always formed as a result of straining metastable austenitic stainless steels. Furthermore, dissolved hydrogen is influencing the amount of strain-induced martensite by reducing the stacking fault energy (SFE) of the material [24,25]. All in all, a tensile test of metastable austenitic stainless steels in hydrogen must be considered as a complex and dynamic process involving microstructural changes, gas–solid transfers and hydrogen–dislocation interactions. For testing metastable austenitic stainless steels, these effects should be taken into consideration. The work presented here is focused on the surface condition of a metastable austenitic stainless steel and its influence on HEE.

2. Experimental

2.1. Sample production

Commercially available semi-finished material of austenitic stainless steel was provided by Deutsche Edelstahlwerke (DEW, Germany). The material was produced by continuous casting with a 265 mm square cross section and subsequently hot rolled in several passes to bars with a final diameter of 30 mm. The chemical composition of the material measured by optical spark emission spectrometry is given in Table 1. To account for macroscopic segregations, samples were machined from the center of the bar material parallel to the rolling direction. This approach ensures a comparable influence of segregations for each specimen. Sample production was performed by wet turning varying the machining parameters to optimize the surface roughness. The bars were machined to cylindric tensile specimens with a gauge length of 30 mm and a diameter of 5 mm. Specifically the linear feed f_n (Fig. 1) exhibits a significant influence on the mean roughness index R_a. A variation of f_n from 0.02 to 0.07 mm/rev results in a non-steady change of R_a, however, all measured values are well below the critical one of 0.8 μm defined by ASTM standard G142-98 for mechanical testing in hydrogen atmosphere (Fig. 2). The final parameter set used for the machining of all tensile samples was defined by a linear feed of $f_n = 0.02$ mm/rev, a radial feed of $a_p = 0.1$ mm/rev, a rotational speed of $n = 2500$ rpm and a cutting speed of $v_c = 50$ m/min. These parameters are assumed to provide least surface influence in the as-machined condition. One can expect a more pronounced influence using a parameter set that leads to higher values of R_a. All samples were machined to the final diameter of 5 mm from the material in the as-delivered state. Half of them were additionally solution-annealed in an industrial vacuum heat treatment furnace equipped with a molybdenum heater for 15 min at 1050 °C and quenched with argon gas at a pressure of 200 kPa. Cooling rates from solution annealing temperature were sufficiently high for all samples to ensure a fully austenitic microstructure free of precipitates. The resulting grain size for both conditions was 50 μm ± 5 μm. Through this processing two different surface conditions were obtained: a martensite-free one for the heat-treated specimens and a condition bearing strain-induced martensite below the surface. The residual oxygen partial pressure of the argon gas used for quenching lead to a visible oxidation of the surface. Therefore, the chemical composition and the thickness of the oxide layers were measured by secondary ion mass spectrometry.

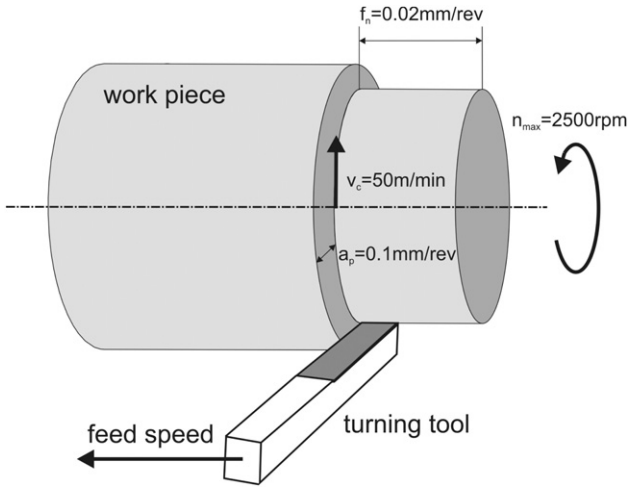

Fig. 1 – Schematic representation of the turning process for machining tensile samples with a defined surface roughness.

Table 1 – Chemical composition of the investigated austenitic stainless steel; values in mass-% with iron being the dependent substitutional element.

C	Si	Mn	P	S	Cr	Ni	Mo	Cu	V	Co	N
0.016	0.68	1.95	0.030	0.031	17.89	8.63	0.30	0.60	0.092	0.102	0.071

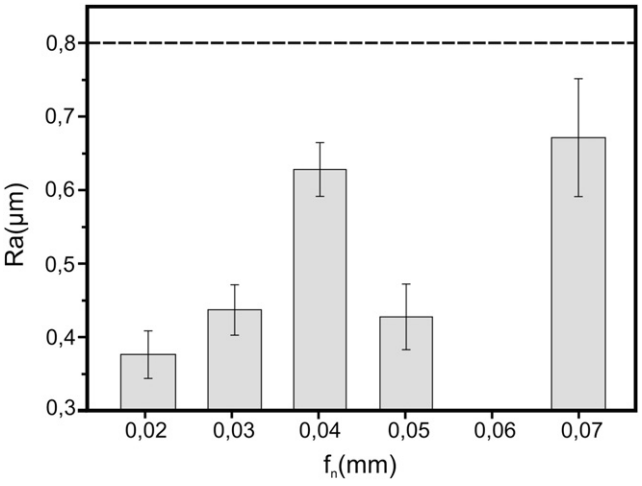

Fig. 2 – Influence of f_n parameter on the surface roughness R_a of as-turned samples. The horizontal line represents the maximum roughness value R_a allowed according to ASTM standard number G142-98.

2.2. Microstructure

For microstructural investigations, radial cross sections were prepared metallographically by cutting and embedding the samples followed by grinding and polishing according to standard preparation routes. For a better optical contrast, samples were finally etched in V2A solution (100 ml H_2O, 100 ml HCl, 10 ml HNO_3). Both, microstructures and fracture surfaces, were investigated by optical microscopy and SEM. Vickers hardness values were obtained by operating a micro hardness tester with a load of 50 g. At least 5 indentations were performed for each measurement. X-ray diffraction was performed in the range of 62–112 2θ with a Siemens D500 diffractometer using Cr-Kα radiation to check for the presence and structure of martensite. Diffraction patters were analyzed in comparison to data of Narita et al. on α- and ϵ-martensite in type 304 steel [26].

2.3. Tensile tests

Two different sets of tensile tests were performed, one in air at room temperature (RT) and the other in pure hydrogen gas ($\geq$99.9999% H_2) at a pressure of 40 MPa and 25 $\pm$ 3 °C. The pressure vessel was purged several times with pure nitrogen gas to minimize oxygen partial pressure. Tensile tests in hydrogen were performed by The Welding Institute (TWI, Cambridge, UK). For these tests, load and elongation were determined by an external load cell and the cross head displacement. The initial strain rate of all tensile tests was 5.5 10^{-5} s^{-1}, being comparable to the value used in Ref. [12]. At room temperature this strain rate is slow enough to expect an influence of hydrogen on the results of the tensile tests. In other words, the strain rate is low enough to allow hydrogen to migrate with moving dislocations. Besides the determination of yield strength, tensile strength and elongation to fracture, the relative reduction of area was measured with a caliper, as this quantity is known to be very sensitive for hydrogen embrittlement [9,27].

2.4. Secondary ion mass spectrometry

To investigate the local chemistry and the element distribution of Ni, Fe, Cr and C in the first 100 nm below the sample surface, secondary ion mass spectrometry (SIMS) was performed. A commercial TOF-SIMS IV from ION-TOF GmbH was used equipped with a time of flight detector (TOF). A background pressure of $1 \cdot 10^{-7}$ Pa was used to prevent surface oxidation during the measurement. Measurements were taken by applying dual beam mode with gallium$^+$ (Ga) and cesium$^+$ (Cs) sources. Negative ions were acquired by applying a Ga^+ primary ion beam operating at 25 keV and 0.1 pA. The sputtering was accomplished by Cs^+ at 1 keV and 2.5 nA screening over 300 $\times$ 300 μm^2 area. Under these conditions, the lateral resolution of the Ga-beam ions is 5 μm. The depth resolution is, for flat surfaces, about 1 nm, slightly increasing with measuring time and sample depth.

Sample machining results in a surface roughness lower than the industrially allowed roughness of 0.8 μm, as defined by ASTM standard G142-98. Profilometer measurements yield surface height variations of 2.4 μm. They appear with a linear lateral extension of about 50 μm at the sample surface, for both solution-annealed and as-machined specimens. This technical surface topography complicates the surface analyses by SIMS affecting mostly the depth resolution. In the measurement, it broadens interface transitions and blurs elemental depth profiles. Profiles taken perpendicular and parallel to the surface topography reveal different depth profiles while those taken parallel show sharper interfaces. Therefore, this condition was adjusted for all measurements. Surface roughness is similar for both conditions, thereby affecting the depth resolution of both conditions in a similar way. To obtain a depth length scale, depth profiles reveal a calibration of the sputter cycle number which depends on the materials resistance against ion sputtering. For these measurements, calibration is based on the known thickness of the native oxide on the as-machined sample, which is about 5 nm. The sputter rate and, consequently, the depth scaling for both samples are based on this calibration. Thus, changes in the sputter rate due to different mechanical hardness of the two samples, related to locally different chemical composition and lattice structures are neglected.

2.5. Calculation of hydrogen diffusion distances

The formation of strain-induced martensite below the surface of as-machined austenitic steels is a well known effect. Being aware of the differences regarding hydrogen permeation between bcc and fcc lattices, a major interest is to evaluate the influence of this α' layer by establishing a direct comparison with the martensite-free (heat-treated) material. Consequently, diffusion calculation at room temperature was performed. In order to do that, permeability (ϕ) and diffusivity (D) values at RT were obtained by extrapolating permeation measurements carried out on ferritic and austenitic stainless steels (SS) [8]. This route served as a conservative approach to hydrogen diffusion in strain-induced martensite and a quite precise one for the austenitic matrix, respectively.

Once a solubility (K) value is obtained as the quotient between permeability and diffusivity (Eq. (1)), hydrogen concentration at the specimen surface C_S can be calculated according to Eq. (2) with f being the corresponding fugacity, assuming Abel-Noble state equation [28] at testing condition (40 MPa, 25 °C).

Subsequently, the solution of Fick's second law for the case of the semi-infinite body has been employed for calculating the hydrogen concentration profile (Eq. (3)), an assumption that leads to minor or small differences in comparison to the exact round bar solution [29]. In this expression, x represents the depth from the surface, C_S the hydrogen surface concentration that is dissolved in the metal lattice and in equilibrium with the hydrogen gas (40 MPa, 25 °C), C_0 the hydrogen content of "as-received" material, D the diffusion coefficient, and t the diffusion time. For the last, a period of 180 s was employed, due to a correspondence to the tensile test elastic regime interval, and the initial concentration (C_0) was assumed equal to zero.

$$K = \phi \cdot D^{-1} \tag{1}$$

$$C_S = K \cdot f^{0.5} \tag{2}$$

$$C(x,\ t) = (C_S - C_0)\cdot\left(1 - erf\left(\frac{x}{2\cdot(D\cdot t)^{0.5}}\right)\right) + C_0 \quad (3)$$

In general, the preceding approximation tends to evaluate the hydrogen distribution below the surface prior to plastic deformation. In this context, it must be emphasized that the kinetics of hydrogen dissociation, superficial oxide layers, as well as trapping effects, have been neglected.

3. Results

3.1. Microstructure

Considering the chemical composition (Table 1) and especially the low nickel content of 8.6 wt.% it becomes clear that the austenitic stainless steel investigated here is a so-called "metastable" austenitic steel, as it is capable of undergoing a strain-induced transformation to α-martensite at room temperature. The low stability of the austenite in this specific case can be mainly attributed to the low amount of nickel, being partly compensated by manganese and nitrogen as austenite stabilizing elements. Thus, the presence of α-martensite below the surface of the as-machined samples can be anticipated. The latter can be seen in Fig. 3, where below the surface and to a depth of 50 μm, martensite was detected metallographically. By X-ray diffraction, α-martensite but no ϵ-martensite was detected (Fig. 4). Certainly, there might be a small fraction of ϵ-martensite present in the microstructure indicated by a shoulder to the right of the α (110) reflection, however, the major phase at the surface is α-martensite. Its presence is also supported by micro hardness measurements (Fig. 5), showing significantly higher values at a distance of 15 μm below the surface. In a depth of 100 μm virtually no hardening effect can be measured compared to the hardness of the bulk. Assuming 100 μm as penetration depth and considering the sample diameter of 5 mm, less than 8% of the samples volume in the initial state is affected by the turning process. In contrary, the group of samples which was solution-annealed at 1050 °C, a temperature at which only the fcc structure is thermodynamically stable, showed a martensite-free subsurface, as depicted in Fig. 6.

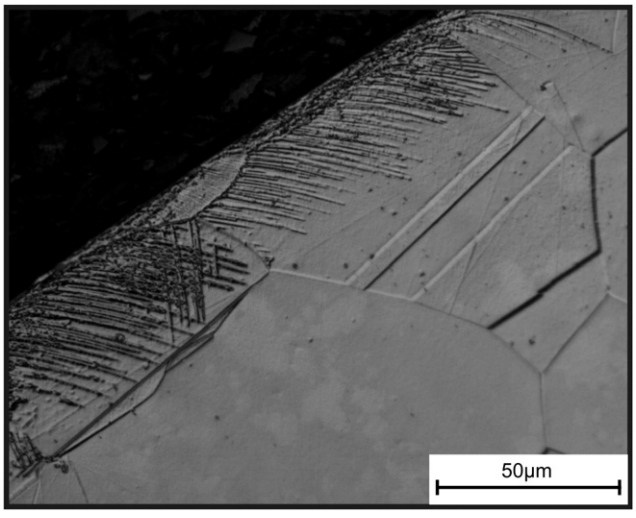

Fig. 3 – Radial cross section of a tensile sample in as-machined condition showing strain-induced martensite formed below the turned surface.

3.2. Tensile tests

For evaluating the results of the tensile tests, only load–displacement curves are used instead of stress–strain curves. This restriction arises from the uncertainties related to a precise measurement of strain in the high-pressure hydrogen atmosphere. Several commercial resistance strain gauges were applied, all of them with a significant error induced by the hydrogen atmosphere. The error related to the comparison of load–displacement curves is small, as all samples were machined on CNC machines with narrow tolerances. In Fig. 7 two exemplary curves of samples of the first batch with and without martensite measured at room temperature in air are depicted. Even though the amount of martensite is low and restricted to a layer of 100 μm thickness at the surface only, slightly higher loads are apparent for the material with martensite. However, the difference in yield and tensile strength obtained in air is negligible (cf. Table 2). For the same batch of samples, Fig. 8 shows two exemplary results of tensile tests performed in hydrogen. Again, higher loads corresponding to higher stresses are measured for the sample containing martensite while the elongation to fracture is reduced. Regarding the several discontinuities ("serrations") as well as the apparent hardening occurring around 5 mm and 10 mm of displacement, it must be noted that both aspects are artifacts. The first one is related to friction between high-pressure seals and moving parts of the tensile testing device, the second one to the data acquisition by an external load cell. The experimental setup for testing in hydrogen, comprising the use of cross head displacement and an external load cell for the measurement of mechanical properties, explains the differences in elastic limit and tensile strength (Table 2). The discussion of results focuses on the relative reduction of area, as it is a sensitive measurement obtained ex situ.

Considering only the load–displacement curves, one might expect an insignificant effect of surface martensite on the tensile properties of metastable austenitic stainless steels. However, the relative reductions of area differ significantly depending on the presence of martensite. In Table 2 results of the material tested in air and in hydrogen are given. Measuring in air does not affect the reduction of are (RA) value while a significant reduction is obtained by testing in hydrogen. Differences in surface appearance and ductility response can be seen in two samples tested in hydrogen at 25 °C (Fig. 9). Especially the number and dimension of secondary cracks appearing on the sample with surface martensite is increased significantly. The distinct formation of secondary cracks is caused by the hydrogen atmosphere, as it is not found on the samples tested in air. Discrepancies in RA become univocal by looking at the fracture surfaces of the specimens shown in Fig. 10. Both samples exhibit localized plasticity and cleavage-like failure but the one without surface martensite shows necking prior to fracture. One should keep in mind that both samples shown in Fig. 10 had the same

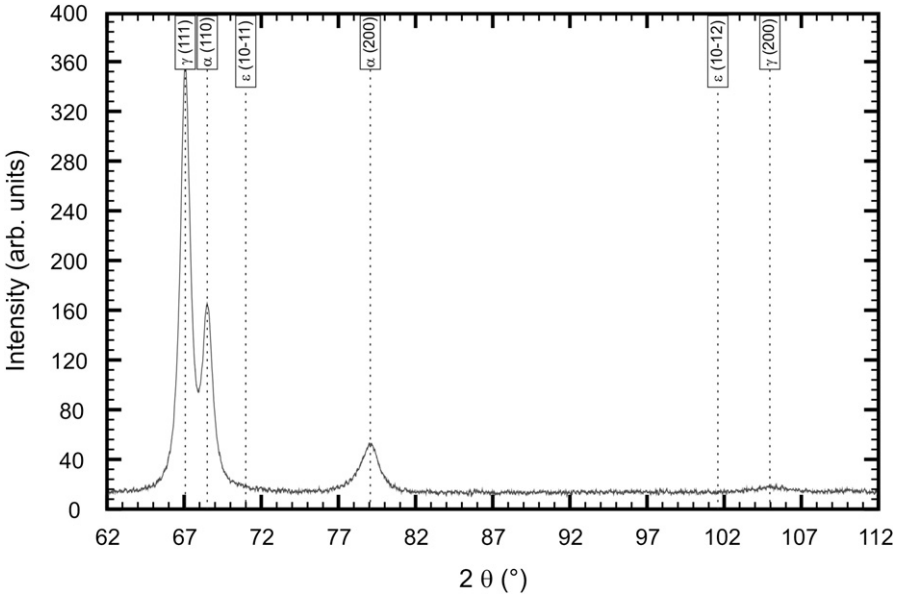

Fig. 4 – X-ray diffraction pattern of as-turned flat surface measured with Cr-Kα radiation.

initial diameter and chemical composition. It can be concluded, that the microstructure of the surface area and specifically the presence of martensite prior to testing in hydrogen influences the results of tensile tests significantly.

3.3. *Secondary ion mass spectrometry*

SIMS experiments were performed to characterize surface oxides and chemical composition. Fig. 11 shows surface depth profiles of the upper 25 nm of the as-machined sample (11a) which consists of about 100 μm thick layer of surface martensite and the as quenched austenitic sample without martensite (11b). The elemental sputter yield is plotted on logarithmic scale as a function of the cycle number. The cycle number is, as described above, transferred to a depth scale. All elements showing a surface distribution different from the homogeneous bulk profile, are plotted. These elements are nickel Ni (60Ni plotted to prevent signal overlap with iron-isotope), iron Fe, chromium Cr, silicon Si, cyanide CN, sulfur S and carbon C. Many elemental ions appear in oxide mode. At the surface these oxides reflect the surface oxide layer. In bulk, the detected intensities relate to surface roughness and element surface oxidation from the background pressure. Si most probably always appears in the oxidized state SiO_2, as Si acts as oxygen getter inside of the steel. Nitrogen N is preferentially detectable in the CNO mode.

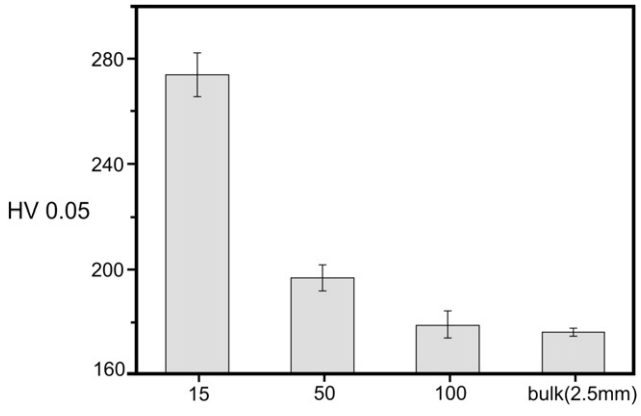

Fig. 5 – Vickers micro hardness measured 15, 50, 100 and 2500 μm below the as-machined surface.

Maximum intensities of the different elements appear in different sample depths. For the as-machined sample containing martensite (Fig. 11a), a maximum Fe signal is detected in the first 2.5 nm. Also, the S signal appears high in this region. In a depth of about 4 nm the Cr signal is high. Below that, at about 4 nm the Ni signal shows its maximum. Ni shows a low intensity shoulder at about 2 nm depths. The Si signal reveals a maximum at about 3.5 nm depth. N shows an increased intensity at the surface. C is distributed randomly, but with a high intensity.

For the Ar quenched sample without martensite (Fig. 11b), the maximum Fe signal is present over the first 6 nm. The S signal is shifted toward the sample interior and reaches its maximum at 7 nm. The Cr intensity has its maximum at 8 nm depth and a shoulder at 3 nm depth. Ni intensity is low for the uppermost layers and reaches its maximum at about 8 nm. The C signal is slightly increased toward the sample surface showing a maximum at 2 nm. The SiO_2 content is nearly constant and higher than in Fig. 11a.

The sequence of intensities can be interpreted as follows, giving estimations for the types of oxides just by naming the most stable types: for both samples the surface is covered with an Fe_2O_3 layer, which is in agreement with literature data on AISI 304 steel [17]. Below this, the stable Cr_2O_3 is detected. Lateral distribution images, not shown here, prove a thin Cr_2O_3 layer for the martensite sample, but a particle-like distribution for the Ar quenched sample [30]. The shoulder in the Cr profile in the austenitic sample might be due to the formation of $FeCrO_3$ during heat treatment. NiO is detected at

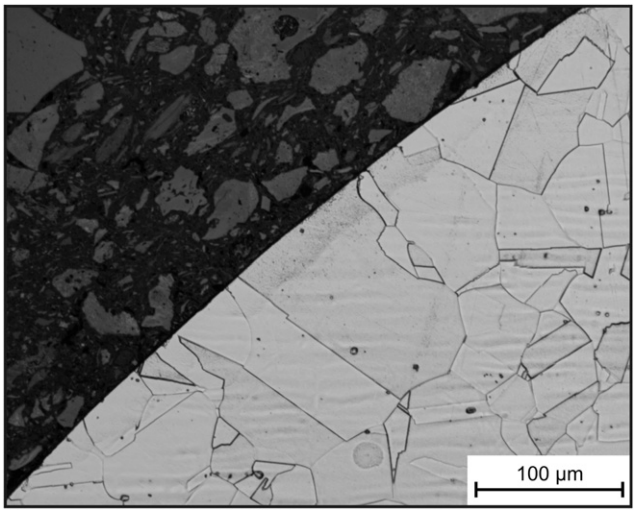

Fig. 6 – Radial cross section of a tensile sample after solution annealing for 15 min at 1050 °C followed by argon gas quenching.

the sample surface for the Ar quenched sample. Summarizing the different types of oxides to one "surface oxide layer" yields about 5 nm of oxide layer, in case of the martensite sample (Fig. 11a), and about 10 nm for the austenite sample (Fig. 11b). Thus, the oxide layer is by a factor of two thicker for the fully austenitic sample.

The high N surface content for the Ar quenched sample could be related to a contamination achieved during Ar quenching. However, since the quenching gas contains less than 10 ppm of N, its influence is supposed to be negligible. Another source for nitrogen is the bulk material itself, containing about 0.07 wt.%. During solution annealing in high vacuum condition nitrogen could be driven to the surface and accumulate there.

Table 2 – Mechanical properties of first batch of samples determined by tensile testing at room temperature in air and hydrogen atmosphere at $p = 40$ MPa.

Condition	Atmosphere	R_p [MPa]	R_m [MPa]	A5 [%]	RA [%]	RRA [%]
as-machined	air	222	645	74.5	82.1	51.6
as-machined	air	213	640	74.1	81.8	
as-machined	H_2	293	605	38.7	30.7	
as-machined	H_2	174	551	75.2	53.9	
solution-annealed	air	211	643	74.4	81.4	84.1
solution-annealed	air	211	642	74.9	81.9	
solution-annealed	H_2	162	549	82.1	70.1	
solution-annealed	H_2	158	525	81.3	67.2	

Also the C signal shows an unexpected behavior: Its bulk content is higher for the martensite containing sample, although similar intensities were expected. The value measured in the martensite is reflecting the carbon content of the metastable austenite prior to strain-induced transformation. In contrary, the surface of the argon quenched sample was exposed to high vacuum conditions during solution annealing treatment. It is a well known effect, that carbon from the bulk material is able to reduce surface oxides in the course of a vacuum heat treatment. Naturally, the surfaces are re-oxidized immediately during quenching and air exposure. However, the reduction could be an explanation for the lower carbon surface concentration of the argon quenched sample.

Lateral element distribution maps, not shown here, prove a Si segregation at grain boundaries leading to the high and homogeneous Si signal in the depth profile [30]. Most probably this also arises from the heat treatment when Si diffuses to the sample surface.

3.4. *Calculation of hydrogen diffusion distances*

Calculated hydrogen diffusion parameters and concentration values are presented in Table 4. As can be seen, at room

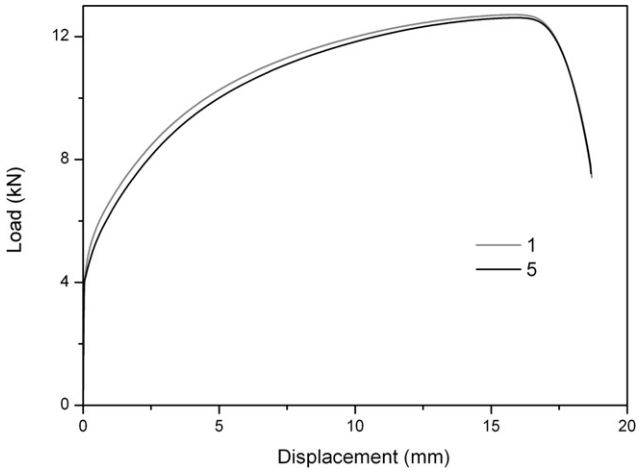

Fig. 7 – Exemplary load–displacement curves of tensile samples with (1) and without (5) surface martensite measured at RT in air ($p = 0.1$ MPa) with an initial strain rate of $5.5 \cdot 10^{-5}$ s^{-1}.

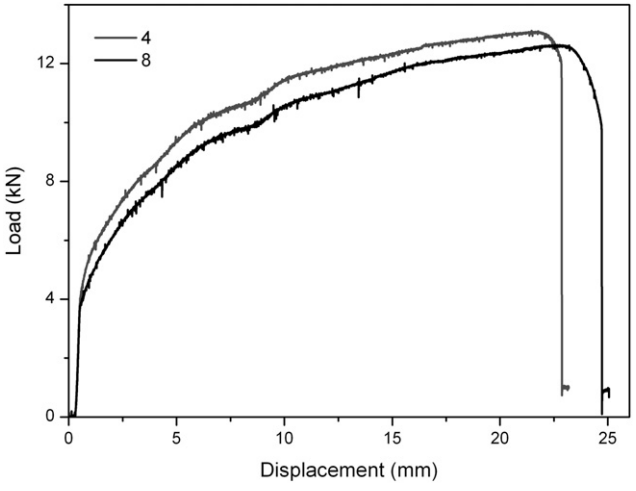

Fig. 8 – Exemplary load–displacement curves of tensile samples with (4) and without (8) surface martensite measured at RT in hydrogen ($p = 40$ MPa) with an initial strain rate of $5.5 \cdot 10^{-5}$ s^{-1}.

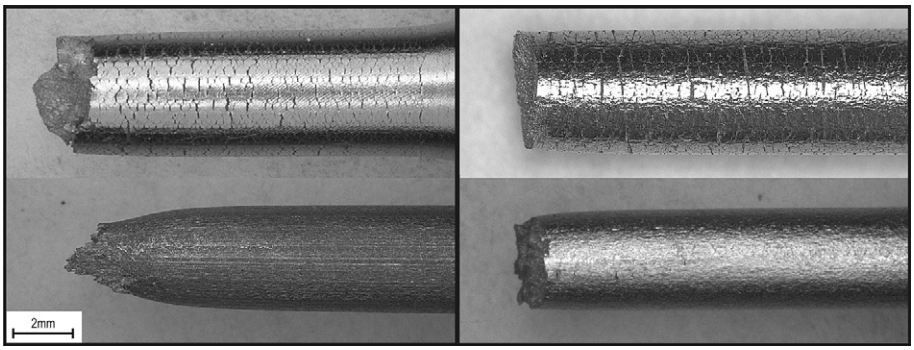

Fig. 9 – Macroscopic view of tensile samples after testing in hydrogen: left: first batch of samples (top: as-machined, bottom: solution-annealed) right: second batch of samples (top: as-machined, bottom: solution-annealed).

temperature hydrogen diffusivity in the bcc structure is five orders of magnitude higher compared to fcc. Additionally, the latter can dissolve 140 times more hydrogen than the bcc lattice. Both results are consistent with general observations for closed-packed structures, characterized by a higher solubility and lower mobility for interstitial elements. Accordingly, a concentration of 0.32 and 45 ppm was obtained as the surface saturated values for the ferrite and austenite phase, respectively. The previous results can be visualized in Fig. 12. As can be seen, hydrogen diffusion is strongly hindered in the fcc lattice, showing an abrupt drop from 45 ppm at the surface to a concentration value of zero in a range of one micron. Hydrogen penetration is more pronounced in the bcc lattice, reaching almost the saturation value at a depth of 10 μm and half of it at a distance of 50 μm from the surface, even though exposure time of 180 s is short.

These calculations suggest that strain-induced martensite is able to facilitate hydrogen entry by means of diffusion and therefore, for slow strain rates, to act as a source of hydrogen for moving dislocations.

4. Discussion

Hydrogen environment embrittlement is an issue of technical importance that might play a role for future energy storage solutions. Austenitic stainless steels are candidate materials specifically for components for mobile applications. Reliable technical solutions exist, either by using high-alloyed, cost-intensive materials like AISI 309/310 or increasing safety factors for construction, but it is still necessary to develop less expensive materials and reduce weight by thin-walled components. As long as hydrogen is not dissolved in the fcc lattice of an austenitic steel, no influence on the mechanical properties can be expected. In the unloaded condition the surface of austenitic stainless steel is protected against uptake of molecular hydrogen by the passivation layer formed immediately at ambient conditions. The restriction to molecular hydrogen arises from the fact that the passive layer hinders dissociation of hydrogen on the surface of the steel. In contrast, the way back, this means from the bulk through the passive layer, is possible [31]. However, once load is applied, either dynamic or static, the passivation layer can be destroyed producing fresh metal surface. A re-passivation can only take place, if sufficient oxygen is supplied. Otherwise, like in the case of this study performed in pure hydrogen, the fresh metal surface is not re-passivated and allows hydrogen to enter the material.

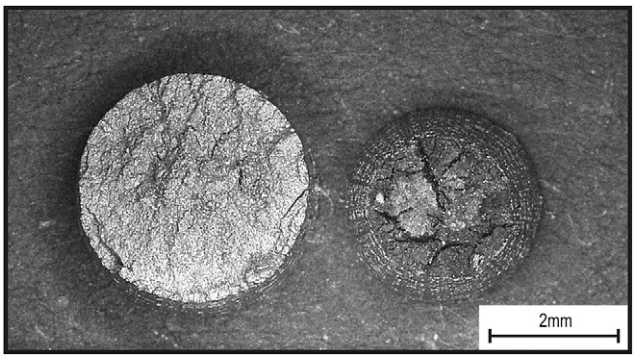

Fig. 10 – Fracture surfaces of two exemplary samples with (left) and without (right) surface martensite after testing in hydrogen atmosphere.

The diffusivity of hydrogen in iron fcc structures is low compared to ferritic steels, as shown in this work by the calculation of penetration depths. As soon as bcc structures are present in the microstructure the situation changes: In bcc iron the diffusivity is by several orders of magnitude higher, even at room temperature, allowing hydrogen to enter along fast diffusion paths [29]. This implies that at least tensile testing of metastable austenitic steels in hydrogen containing atmospheres is a highly dynamic process.

In order for external hydrogen to assist fracture, three consecutive stages have to be covered at the testing conditions used in this work: rupture of the passivation layer, crack initiation at the surface and crack propagation [32]. In addition, the diffusion of hydrogen into the lattice is a condition, that has to be considered for testing hydrogen-free material in a hydrogen atmosphere. For the first stage, no difference is expected between the as-machined and the solution-annealed state. This can be deduced from the similarities in thickness and chemical composition of the passivation layers characterized by SIMS measurements. The oxide on the annealed and argon quenched sample is twice as thick as on the as-machined one, but, with only 10 nm, it is still a thin

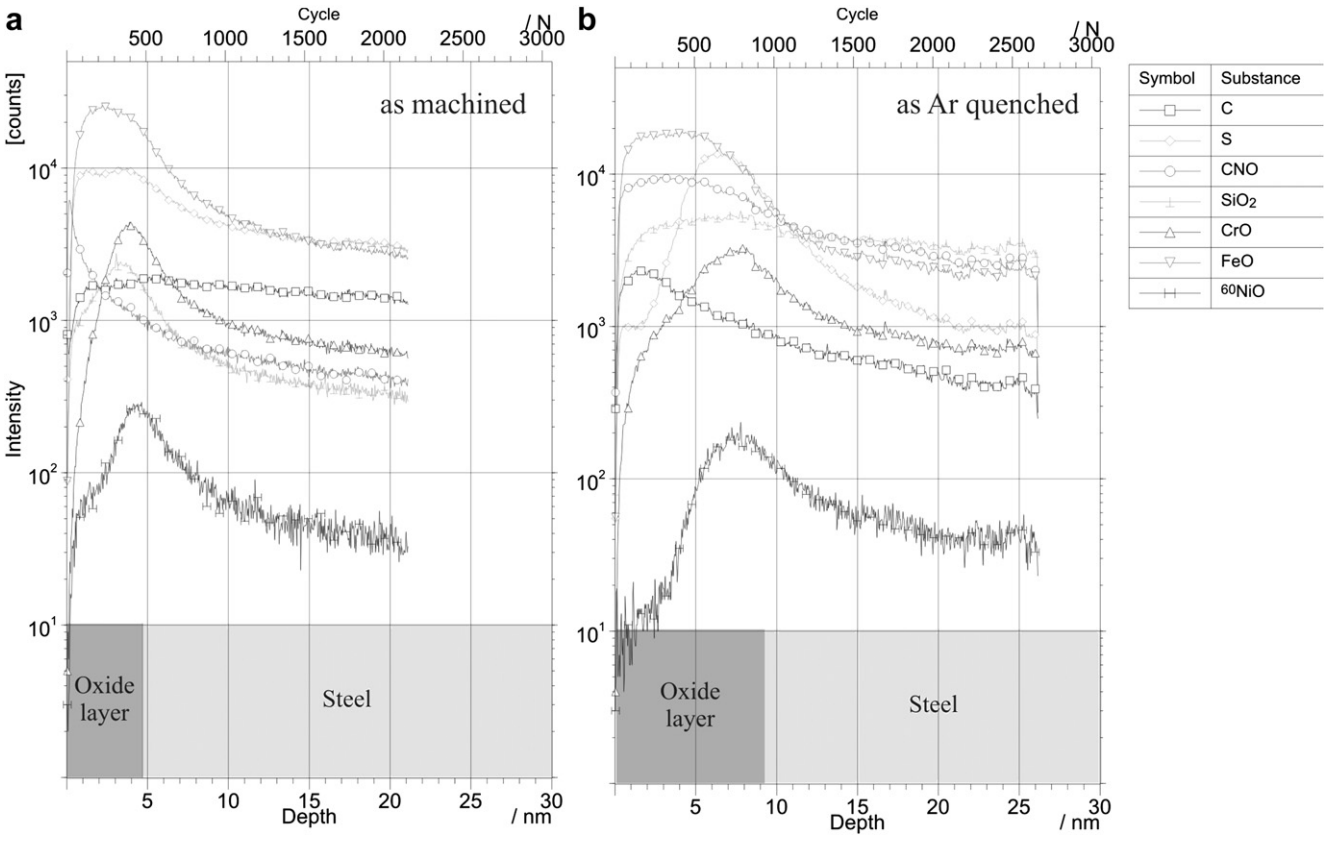

Fig. 11 – Surface depth profiles of alloying elements of samples with (left) and without (right) surface martensite.

layer. The chemical composition of the steel side at the interface oxide/steel is the same except for the carbon content (cf. Fig. 11). This means, once the oxide layer was damaged due to straining the sample, molecular hydrogen encounters comparable chemical conditions except the difference in crystallographic structure.

A major difference can be anticipated regarding the formation of superficial cracks ("secondary cracks"). For the as-machined state, diffusion calculations show that hydrogen is capable to almost saturate ferrite at room temperature to a depth of 100 μm within 180 s. The temperature corresponds to the experimental conditions applied in this work, while the time was chosen according to the extent of elastic straining during the tensile test. Localized failure of the passive layer by elastic deformation is assumed here. With this assumption, the calculated penetration depths show that hydrogen is able to saturate the whole layer of α-martensite before plastic deformation is initiated. In addition, the pre-existing machining-induced martensite can serve as a nucleation site for strain-induced martensite formed during tensile testing [33,34], and consequently, is able to extend the range for hydrogen penetration. At the low strain rates applied here, hydrogen is able to follow the martensite freshly formed by autocatalytic nucleation.

In this context, the interface between martensite laths and the austenitic matrix plays a decisive role. As the interface has to accommodate the mismatch between both structures, the

Table 3 – Mechanical properties of second batch of samples determined by tensile testing at room temperature in air and hydrogen atmosphere at $p = 40$ MPa.

Condition	Atmosphere	R_p [MPa]	R_m [MPa]	A5 [%]	RA [%]	RRA [%]
as-machined	air	223	632	74.0	82.2	30.6
as-machined	air	232	643	75.4	82.0	
as-machined	H_2	232	544	35.7	22.9	
as-machined	H_2	234	545	38.7	27.4	
solution-annealed	air	223	650	72.3	81.0	53.2
solution-annealed	air	217	632	74.4	80.8	
solution-annealed	H_2	216	605	65.5	40.3	
solution-annealed	H_2	212	642	69.3	45.8	

Table 4 – Transport parameters and hydrogen concentration in ferritic and austenitic stainless steel in contact with hydrogen gas (40 MPa, 25 °C); calculated values based on data published in Ref. [8].

Material	D [$m^2\ s^{-1}$]	ϕ $\left[\frac{mol_{H_2}}{m\ s\ MPa^{0.5}}\right]$	K $\left[\frac{mol_{H_2}}{m^3\ MPa^{0.5}}\right]$	C_S [ppm]
Ferritic SS	1.05E-11	1.83E-12	0.17	0.32
Austenitic SS	3.50E-16	8.58E-15	24.55	45.02

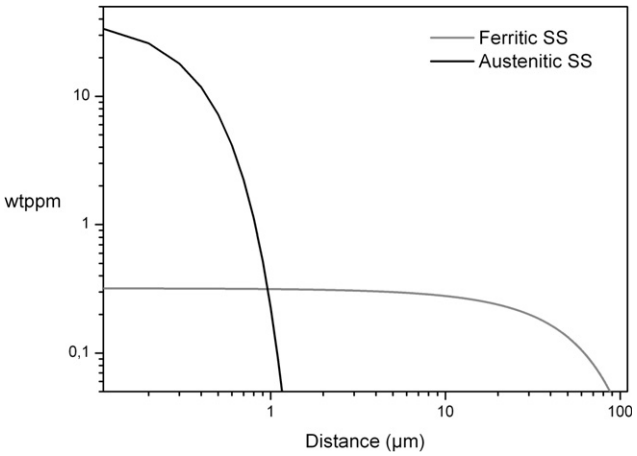

Fig. 12 – Diffusion calculation for ferritic and austenitic stainless steel subjected to a 40 MPa, 25 °C hydrogen gas atmosphere for 180 s.

resulting higher strain and dislocation density can enhance the local hydrogen concentration at the phase boundary. In this way, proper conditions for the hydrogen enhanced localized plasticity (HELP) mechanism to operate are generated. Hydrogen enhanced localized deformation can take place at the $\alpha-\gamma$ interface, leading to microcrack generation which later on can propagate along the martensite laths and form superficial cracks. In this regard, the formation of microcracks in the presence of hydrogen at microstructural interfaces in austenitic stainless steel has already been reported in Ref. [35]. Thus, α-martensite is mainly affecting the kinetics of the embrittlement process by an immediate initiation of superficial cracks, as it can be clearly seen on the surfaces depicted in Fig. 9.

On the contrary, in the solution-annealed condition the superficial cracks are initiated after necking has already occurred. Once superficial cracks are generated, the tensile test evolves as fracture toughness test. The surrounding high-pressure H_2 gas gets in contact with the freshly opened fracture surfaces, hydrogen can diffuse and concentrate at the plastically deformed and elastically strained crack tip, enhancing localized deformation which facilitates crack propagation. The latter is expected to be assisted by a localized formation of α-martensite at the crack tip as it has been shown in fracture toughness tests of AISI type 304 steel [36]. Finally, those cracks which face higher stresses will propagate faster and lead to the failure of the specimen.

An aspect that was neglected in the discussion of the results so far is the presence of a visible oxide layer on top of the heat-treated and martensite-free sample. According to the results of SIMS, its thickness is twice the value of the as-machined sample but it can still be treated as a thin layer. It can be argued, that the thicker oxide layer also plays a role for hydrogen uptake in the course of a tensile test, even tough fracture of the passive layer or an artificial oxide layer by straining is frequently found in literatures [22,23]. Looking at the results of tensile tests in air and hydrogen (Table 2), an abnormal scatter of yield strength is encountered. To verify the results discussed so far, a second batch of samples taken from the same heat was investigated. Both, vacuum heat treatment and tensile testing in high-pressure hydrogen, were revised and optimized. Unlike the first batch of samples, the second batch was austenitized for 30 min instead of 15 min at 1050 °C. Tensile tests with the same parameters as before were performed in air and 40 MPa hydrogen for both conditions, with and without martensite. The results of these tests are given in Table 3 and show the same trend as the first batch of samples but without a significant scatter of yield and tensile strength. Again, the samples containing machining-induced martensite exhibit less elongation to fracture and less reduction of area. Furthermore, the surfaces of the samples containing machining-induced martensite also exhibit a significantly higher number of secondary cracks after testing in hydrogen (cf. Fig. 9). Comparing first and second batch, the difference in RRA varies: For the first batch, RRA values of 84.1% and 51.5% were found, for the second batch the values are 53.2% and 30.6% without and with machining-induced martensite, respectively. The difference can either be attributed to the thicker oxide layer on the first batch of samples or a difference in surface composition as a result of the extended dwell in vacuum during austenitization. This question is still open and will be considered in further investigations. However, the general result is still clearly visible: The presence of a layer of machining-induced martensite is detrimental for HEE. This result and its interpretation is consistent with works of Brass et al. who investigated the influence of shot-peening on hydrogen embrittlement of AISI 304 steel [38]. Even though the material the authors investigated contained 0.8 wt.% more nickel than the one studied here, they found that shot-peening has a detrimental influence on susceptibility to HEE and related this result to the presence of α-martensite. Clearly, shot-peening is not the same as machining, but the resulting microstructure below the surface is almost the same and contains a high amount of α-martensite due to plastic deformation. Furthermore, secondary cracks were predominantly found on shot-peened surfaces after testing in hydrogen and to a lower extent on the reference samples.

5. Conclusions

The results obtained in this study reveal the distinct influence of a comparatively thin surface layer of machining-induced martensite on the mechanical properties measured in pure hydrogen. The relative elongation to fracture and the relative reduction of area (RRA) are often used as sensitive measures for the amount of HEE. Specifically for metastable austenitic steels with 8–10 wt.% nickel, the scatter of experimental values is large [1,37]. The authors hold the opinion, that this scatter is not only related to segregation effects, differences in bulk chemical composition and different production routes, but also to the surface microstructure of the material tested. In case of martensite initially being present, a lower relative elongation to fracture and a lower RRA are measured compared to a martensite-free surface. Of course, in scientific works the surfaces of samples are usually ground and polished after machining to remove martensite and other surface artifacts. However, for technical hydrogen applications of metastable austenitic

stainless steels, especially of complex shaped parts, grinding or polishing might not be possible or too expensive. The chemical alternative of pickling should also be handled with care, as it can introduce hydrogen into the material, too. A final heat treatment can be an appropriate solution, as is removes machining-induced martensite completely. According to this study, a slight oxidation of the surface during this heat treatment is not detrimental concerning HEE. Quite the contrary, comparing the result of the first and the second batch of samples, a slightly thicker oxide layer can be assumed to have a positive influence on HEE.

Therefore, for testing metastable austenitic stainless steels in hydrogen atmosphere, surface martensite in the initial state of the samples should be avoided. In the same manner, technical surfaces supposed to be in contact with hydrogen should be kept free of martensite either by heat treatment or an alternative surface conditioning.

6. Summary

In this work an AISI type 304 metastable austenitic stainless steel was tensile tested in air and hydrogen at 40 MPa and room temperature. Two different surface states of the tensile samples were investigated, namely argon quenched without α-martensite and as-machined with martensite below the surface to a depth of about 100 μm. The most sensitive parameter for hydrogen environment embrittlement, the relative reduction of area (RRA), was found to decrease significantly due to the presence of martensite at the surface. The authors draw the conclusion that the immediate formation of superficial cracks resulting from the presence of machining-induced martensite accelerates the embrittlement process and leads to a premature failure in comparison to the same, but martensite-free, material.

Acknowledgment

The authors gratefully acknowledge the financial support of the Bundesministerium für Wirtschaft und Technologie (BMWi) under contract number 0327802D. Tensile tests in hydrogen were performed at “The Welding Institute” (TWI, Cambridge, UK). Solution annealing treatment was carried out by Dr.rer.nat. S. Yurchenko at the Chair of Materials Technology-TU Dortmund, Germany.

REFERENCES

[1] Michler T, Lee Y, Gangloff RP, Naumann J. Influence of macro segregation on hydrogen environment embrittlement of SUS 316l stainless steel. International Journal of Hydrogen Energy 2009;34(7):3201–9.
[2] Gray HR. Hydrogen embrittlement testing, vol. 543. ASTM Spec. Techn. Publ; 1974.
[3] Singh S, Altstetter C. Effects of hydrogen concentration on slow crack-growth in stainless-steels. Metallurgical Transactions A 1982;13(10):1799–808.
[4] Gavriljuk VG, Stein G, Berns H. Structural stability of austenitic CrMn(Mo)N steels for high-strength, corrosion-resistant retaining rings: corrosion-resistant retaining rings. Steel Research 2003;74(7):444–52.
[5] Shivanyuk VN, Foct J, Gavriljuk VG. On a role of hydrogen-induced epsilon-martensite in embrittlement of stable austenitic steel. Scripta Materialia 2003;49(6):601–6.
[6] Teus SM, Shyvanyuk VN, Gavriljuk VG. Hydrogen-induced gamma-epsilon transformation and the role of epsilon-martensite in hydrogen embrittlement of austenitic steels. Materials Science and Engineering A-Structural Materials Properties Microstructure and Processing 2008;497(1–2): 290–4.
[7] Perng TP, Altstetter CJ. Comparison of hydrogen gas embrittlement of austenitic and ferritic stainless-steels. Metallurgical and Materials Transactions A-Physical Metallurgy and Materials Science 1987;18(1):123–34.
[8] Perng TP, Altstetter CJ. Effects of deformation on hydrogen permeation in austenitic stainless-steels. Acta Metallurgica 1986;34(9):1771–81.
[9] Han G, He J, Fukuyama S. Effect of strain-induced martensite on hydrogen environment embrittlement of sensitized austenitic stainless steels at low temperatures. Acta Materialia 1998;46(13):4559–70.
[10] Perng TP, Altstetter CJ. Hydrogen effects in austenitic stainless-steels. Materials Science and Engineering A 1990; 129(1):99–107.
[11] Michler T, Naumann J. Hydrogen embrittlement of Cr–Mn–N austenitic stainless steels. International Journal of Hydrogen Energy 2010;35(3):1485–92.
[12] Zhang L, Wen M, Imade MEA. Effect of nickel equivalent on hydrogen gas embrittlement of austenitic stainless steels based on type 316 at low temperatures. Acta Materialia 2008; 56(14):3414–21.
[13] Lecoester F, Chene J, Noel D. Hydrogen embrittlement of the Ni-base alloy 600 correlated with hydrogen transport by dislocations. Materials Science and Engineering A-Structural Materials Properties Microstructure and Processing 1999; 262(1–2):173–83.
[14] Gavriljuk VG, Shyvanyuk VN, Teus SM. Hydrogen brittleness of austenitic steels. Materials Science Forum 2010;638–642: 104–9, doi:10.4028/www.scientific.net/MSF.638-642.104.
[15] Sun D, Han G, Vaodee S, Fukuyama S, Yokogawa K. Tensile behaviour of type 304 austenitic stainless steels in hydrogen atmosphere at low temperatures. Materials Science and Technology 2001;17(3):302–8.
[16] Birnbaum HK, Sofronis P. Hydrogen-enhanced localized plasticity – a mechanism for hydrogen-related fracture. Materials Science and Engineering A-Structural Materials Properties Microstructure and Processing 1994;176(1–2): 191–202.
[17] Ferreira MGS, Hakiki NE, Goodlet G, Faty S, P Simoes AM, et al. Influence of the temperature of film formation on the electronic structure of oxide films formed on 304 stainless steel. Electrochimica Acta 2001;46:3767–76.
[18] Izawa C, Uchida HH, Okuhira H, Nishi Y. Hydrogen absorption of LaNi5 after LiOD treatment and surface characterization by TOF-SIMS. Applied Surface Science 2003; 203:665–8.
[19] Borchers C, Michler T, Pundt A. Effect of hydrogen on the mechanical properties of stainless steels. Advanced Engineering Materials 2008;10(1–2):11–23.
[20] Grabke HJ. Reaktion von Ammoniak, Stickstoff und Wasserstoff an der Oberfläche von Eisen. Berichte der Bunsengesellschaft 1968;72(4):541–8.
[21] Barthélémy H. Effects of pressure and purity on the hydrogen embrittlement of steels. International Journal of Hydrogen Energy 2011;36(3):2750–8.

[22] Michler T, Naumann J. Coatings to reduce hydrogen environment embrittlement of 304 austenitic stainless steel. Surface and Coatings Technology 2009;203:1819–28.
[23] Yang Q, Luo JL. Effects of hydrogen and tensile stress on the breakdown of passive films on type 304 stainless steel. Electrochimica Acta 2001;46:851–9.
[24] Whiteman MB, Troiano AR. The influence of hydrogen on the stacking fault energy of an austenitic stainless steel. Physica Status Solidi 1964;7(2):K109–10.
[25] Pontini Adriana Estela, Hermida JD. X-ray diffraction measurement of the stacking fault energy reduction induced by hydrogen in an AISI 304 steel. Scripta Materialia 1997; 37(11):1831–7.
[26] Narita N, Altstetter CJ, Birnbaum HK. Hydrogen-related phase transforamtions in austenitc stainless steels. Metallurgical Transactions A 1982;13A:1355–65.
[27] Louthan Rawl, Caskey GR, Donovan JA. Hydrogen embrittlement of metals. Materials Science and Engineering 1972;10(6):357.
[28] Marchi CS, Somerday BP, Robinson SL. Permeability, solubility and diffusivity of hydrogen isotopes in stainless steels at high gas pressures. International Journal of Hydrogen Energy 2007;32(1):100–16.
[29] Kanezaki T, Narazaki C, Mine Y, Matsuoka S, Murakami Y. Effects of hydrogen on fatigue crack growth behavior of austenitic stainless steels. International Journal of Hydrogen Energy 2008;33(10):2604–19.
[30] Izawa C, Wagner S, Martin M, Weber S, Bourgeon A, Pargeter R, Michler T, Pundt A. SIMS study on the surface chemistry of stainless steel AISI 304 cylindrical tensile test samples showing hydrogen embrittlement, Journal of Alloys and Compounds 2011, in press, doi:10.1016/j.jallcom.2010.12.143
[31] Yang Q, Luo JL. The effects of hydrogen on the breakdown of passive films formed on type 304 stainless steel. Thin Solid Films 2000;371:132–9.
[32] San Marchi C, Michler T, Nibur KA, . Somerday BP. On the physical differences between tensile testing of type 304 and 316 austenitic stainless steels with internal hydrogen and in external hydrogen. International Journal of Hydrogen Energy 2010;35(18):9736–45.
[33] Olson GB, Cohen M. A perspective on martensitic nucleation. Annual Review of Materials Science 1981;11:1–30.
[34] Olson GB, Cohen M. General mechanism of martensitic nucleation 2: fcc-bcc and other martensitic transformations. Metallurgical Transactions A-Physical Metallurgy and Materials Science 1976;7(12):1905–14.
[35] Nibur KA, Somerday BP, Balch DK, San Marchi C. The role of localized deformation in hydrogen-assisted crack propagation in 21Cr–6Ni–9Mn stainless steel. Acta Materialia 2009;57(13):3795–809.
[36] Murakami Y, Kanezaki T, Mine Y. Hydrogen effect against hydrogen embrittlement. Metallurgical and Materials Transactions A-Physical Metallurgy and Materials Science 2010;41A(10):2548–62.
[37] Caskey GR. Hydrogen degradation of ferrous alloys: hydrogen effects in stainless steel. Park Ridge, NJ: Noyes Publications; 1985.
[38] Brass AM, Chêne J, Anteri G, Ovejero-Garcia J, Castex L. Role of shot-peening on hydrogen embrittlement of a low-carbon and a 304 stainless steel. Journal of Materials Science 1991; 26:4517–26.